

# Politecnico di Milano

## Spacecraft Attitude Dynamics Academic Year 2023/2024

### Project group n. 51

### Project n. 499

Team members:

Person code	Surname	Name	Bachelor (type and University)
10711395	Barbiera	Andrea	Mechanical Engineering, Politecnico di Milano
10694949	De Luca	Leo	Mechanical Engineering, Politecnico di Milano
10987083	Perusini	Gianluca	Mechanical Engineering, Swansea University
11013026	Poverini	Viola	Aerospace Engineering, La Sapienza

Project specifications:

	Assigned specification	Modifications (if any)	Motivation for modification
Platform	Microsat (10-100kg)	/	
Attitude parameters	Euler Angles	/	
Mandatory sensor	Gyroscopes	+ Sun sensor, Horizon sensor	To compute attitude determination
Actuators	CMG	/	

## Table of Contents

1.	Project Introduction.....	1
1.1.	Orbit characteristics: .....	1
1.2.	Initial conditions: .....	2
2.	Spacecraft Characteristics .....	2
3.	Spacecraft Attitude Dynamics .....	4
4.	Spacecraft Attitude Kinematics .....	4
5.	Attitude Perturbations .....	5
5.1.	Gravity Gradient:.....	5
5.2.	Solar Radiation Pressure:.....	5
5.3.	Magnetic Field: .....	5
5.4.	Air Drag:.....	6
5.5.	Disturbances' Behaviour: .....	7
6.	Attitude Sensing.....	8
6.1.	Gyroscopic Sensors:.....	8
6.2.	Horizon Sensors: .....	8
6.3.	Sun Sensors: .....	9
7.	Attitude Determination .....	9
8.	Actuator Modelling .....	10
9.	Attitude Control .....	11
9.1.	De-tumbling: .....	11
9.2.	Slew-Manoeuvre: .....	11
9.3.	Earth Pointing: .....	12
10.	Block Diagram .....	13
11.	Simulation Results: .....	13
11.1.	Pointing error, absolute pointing error and relative pointing error: .....	13
11.2.	General results: .....	14
11.3.	Uncontrolled simulation: .....	16
12.	Conclusion: .....	19
13.	References: .....	20

# 1. Project Introduction

In light of the outbreak of modern small sats in recent years and their applications in earth observation, the aim of the project is to simulate the attitude dynamics and control loop of an Earth-pointing Microsat, along with a De-tumble and a Slew maneuver.

To allow for the global coverage of the Earth, a near-polar orbit was chosen, with the vision of a constellations of Microsat distributed in more orbital planes. It was hypothesised that the main mission requirement was to control the satellite in order to observe the evolution of the polar cap, for scientific research in the field of global warming.

The pointing requirement selected for the mission was a low precision pointing with a maximum of 1 *deg* and a lower bound of 0.1 *deg*.<sup>[1]</sup>

The group report is set to present the decisions made and the methods used to model the attitude dynamics, kinematics, environment, sensors, actuators, and control system; in order to then analyze the results of the simulations.

## 1.1. Orbit characteristics

Given the previous considerations, a Low Earth Orbit (LEO) sun-synchronous was chosen, such that the spacecraft could always have the Sun in the sensors' field of view.

Furthermore, the launch was assumed to occur during the spring equinox, with this condition after the de-tumbling of the satellite, the batteries can be recharged by deploying the panels with the normal parallel to the pitch axis of the Local Horizontal Local Vertical (LHLV) reference frame. The orbit was characterized with the values shown in Table 1.

**Table 1: Orbital Parameters**

<b>a</b> [km]	<b>e</b> [-]	<b>i</b> [deg]	<b><math>\Omega</math></b> [deg]	<b>w</b> [deg]	<b>f0</b> [deg]
7259	0.001	97.27276	90	0	0

The selected orbit and its ground track for a period of 5 orbits are shown in Figures 1 and 2.

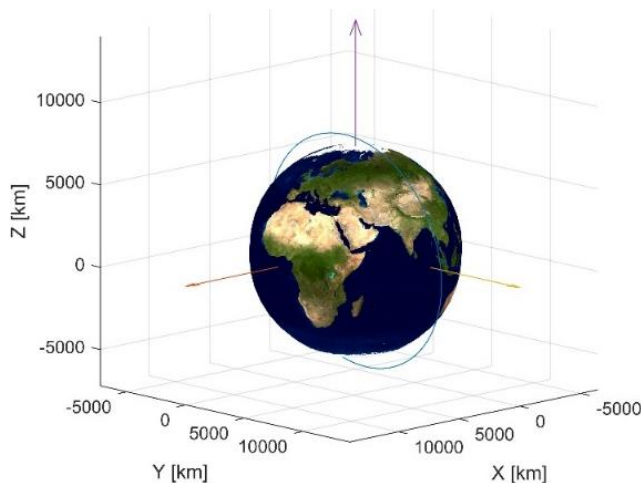


**Figure 1: Microsat's orbit**

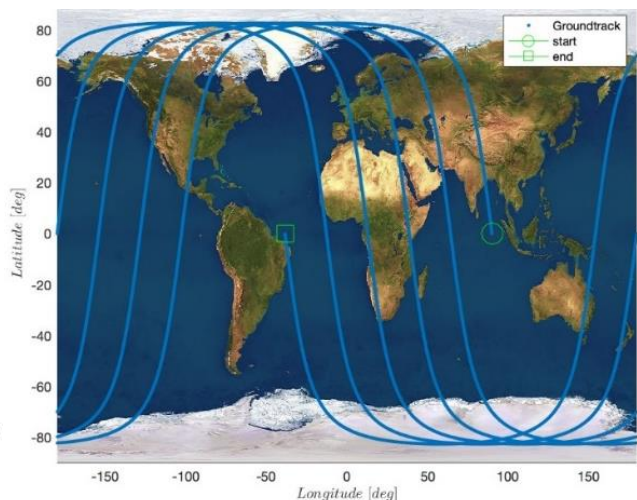


**Figure 2: Ground track of the Microsat**

## 1.2. Initial conditions

The evaluation of the initial values for both the angular velocity and the position of the spacecraft was conducted referring to the data of the launcher manual of VEGA. [2] From its data it was possible to define the initial angular velocity values, as the launcher mechanism's behaviour was defined.

On the other hand, for the initial attitude, there was no guarantee that the satellite would have been aligned to the LHLV frame. Because of this, the initial attitude was represented as three large Euler angles that represent a general orientation after the release from the launcher. The values for the initial conditions are shown in Table 2 and Table 3.

**Table 2: Initial conditions for Angular Velocity.**

wx [deg/s]	wy [deg/s]	wz [deg/s]
2	2	2

**Table 3: Initial conditions for Euler Angles.**

Phi [deg]	Theta [deg]	Psi [deg]
120	120	120

## 2. Spacecraft Characteristics

The spacecraft characteristics were chosen (within the constraints) by observing the LAPAN-A2 microsatellite of Indonesia for earth observation [3]. An image of the Microsat can be seen in Figure 3.



**Figure 3: Starting design for the satellite.**

For our physical model, a few changes were applied to fit the mission and desired shape. For example, the dimensions were switched to have a maximum inertia moment on the Z axis. The overall spacecraft characteristics can be seen in Table 4.

**Table 4: Satellite's Dimensions**

Mass (kg)	Dimensions (m)		
	x axis	y axis	z axis
75	0.5	0.47	0.36

After the definition of the dimensions, the principal inertia moments were computed. Since the satellite has an intrinsic symmetry, the principal inertia axes could be assumed to be coincident to the symmetry axes. Furthermore, the body frame of the Microsat was defined coincident to the principal inertia axes, and the principal inertia matrix was completed:

$$I = \begin{bmatrix} m \frac{y^2 + z^2}{12} & 0 & 0 \\ 0 & m \frac{x^2 + z^2}{12} & 0 \\ 0 & 0 & m \frac{x^2 + y^2}{12} \end{bmatrix} [kg \, m^2]$$

Where all the data was extracted from Table 4:

- $m$  is the mass of the satellite.
- $x \, y \, z$  are the satellite's dimensions.

The solar panels have been selected from the Sparkwing factory models in order to grant a fast recharge of the batteries and to not jeopardize the principal inertia moments of the spacecraft [4]. The dimensions and weight of the solar panels are shown in Table 5.

**Table 5: Solar Panel's Size and Mass**

Mass (kg)	Dimensions (m)		
	Length	Width	Thickness
1.596	0.7	0.6	-

The mass was computed from the formula provided by the constructor itself, which also considered the gimble mechanism to deploy the panels.

The inertia of the panels was added to the one of the Microsat by implementing the Huygens-Steiner theorem.

$$I_{tot} = \begin{bmatrix} 3.4133 & 0 & 0 \\ 0 & 3.5606 & 0 \\ 0 & 0 & 4.2616 \end{bmatrix} [kg \, m^2]$$

Moreover, the optical properties of both the panels and the body of the satellite have been evaluated in the hypothesis that, with respect to the solar radiation, no transmission was allowed by the materials. So, the only optical characteristics that were considered were:

- Diffused reflection:  $\rho_d$
- Specular reflection:  $\rho_s$
- Absorption:  $\rho_a$

The values for the optical coefficients for the body and the panels is shown in Table 6.

**Table 6: Values of optical coefficients**

	$\rho_d$	$\rho_s$	$\rho_a$
Body	0.6	0.1	0.3
Panels	0.1	0.1	0.8

### 3. Spacecraft Attitude Dynamics

With the use of the principal moments of inertia and the initial conditions of the spacecraft, the spacecraft dynamics were modelled using Euler's equations for rotational rigid bodies which were coupled with the dynamic behaviour of the actuators.

$$\begin{cases} I\dot{\underline{\omega}} + \underline{\omega} \times I\underline{\omega} + \dot{A}\underline{h}_r + \underline{\omega} \times A\underline{h}_r = \underline{T} \\ \underline{M}_c = -\dot{A}\underline{h}_r - \underline{\omega} \times A\underline{h}_r \end{cases} \quad (1)$$

The models of the disturbances and the actuators are discussed in the following paragraphs.

### 4. Spacecraft Attitude Kinematics

The kinematics were simulated using Euler Angles and accounting for the presence of singularities. To achieve this, the combinations 312 and 313 were modelled using the equations (1) and (2).

$$\begin{cases} \dot{\phi}_{312} = \frac{\omega_z \cos(\psi) - \omega_x \sin(\psi)}{\cos(\theta)} \\ \dot{\theta}_{312} = \omega_x \cos(\psi) + \omega_z \sin(\psi) \\ \dot{\psi}_{312} = \omega_y - [\omega_z \cos(\psi) - \omega_x \sin(\psi)] \frac{\sin(\theta)}{\cos(\theta)} \end{cases} \quad (1) \quad \begin{cases} \dot{\phi}_{313} = \frac{\omega_x \sin(\psi) - \omega_y \cos(\psi)}{\sin(\theta)} \\ \dot{\theta}_{313} = \omega_x \cos(\psi) + \omega_y \sin(\psi) \\ \dot{\psi}_{313} = \omega_z - [\omega_x \sin(\psi) - \omega_y \cos(\psi)] \frac{\cos(\theta)}{\sin(\theta)} \end{cases} \quad (2)$$

It can be observed that the solutions reach a singularity for different angles of  $\theta$ :  $\cos(\theta) = 0$  for the 312 and  $\sin(\theta) = 0$  for the 313 equations. The switch was designed to activate whenever theta got within a range of  $\frac{\pi}{40}$  from its singularity.

To prevent an algebraic loop when checking for singularities, the state port tool, developed by MATLAB for this purpose, was utilized to calculate the integrated values at a previous time step. Its correct functioning was verified by testing different switches and analyzing the evolution of the angles in time. Using this feature along with enabled subsystems allowed to complete a correct calculation of the kinematics at each time step [5].

The overall DCM was computed by taking the product of the three elementary matrices and multiplying them in the inverse order; this is shown in the equations (3) and (4).

$$A_{312}(\phi, \theta, \psi) = A_2(\psi)A_1(\psi)A_3(\phi) \quad (3)$$

$$A_{313}(\phi, \theta, \psi) = A_3(\psi)A_1(\psi)A_3(\phi) \quad (4)$$

When switching from one combination to another, the initial values were recalculated using equations (5) and (6) extracting the appropriate angles from the last valid DCM. To avoid sign ambiguity, the block atan2 was used when extracting all angles.

$$\begin{cases} \phi_{313} = \text{atan}\left(\frac{A_{31}}{A_{32}}\right) \\ \theta_{313} = \text{atan}\left(\frac{\sqrt{A_{31}^2 + A_{32}^2}}{A_{33}}\right) \\ \psi_{313} = \text{atan}\left(\frac{A_{13}}{A_{23}}\right) \end{cases} \quad (5) \quad \begin{cases} \phi_{312} = -\text{atan}\left(\frac{A_{21}}{A_{22}}\right) \\ \theta_{312} = \text{atan}\left(\frac{\sqrt{A_{31}^2 + A_{32}^2}}{A_{33}}\right) \\ \psi_{312} = -\text{atan}\left(\frac{A_{13}}{A_{23}}\right) \end{cases} \quad (6)$$

## 5. Attitude Perturbations

A model of the environment was completed to analyze the following sources of disturbing torques on the spacecraft:

- Gravity Gradient
- Solar Radiation Pressure
- Magnetic Field
- Air Drag

### 5.1. Gravity Gradient

This is a torque caused by the non-uniformity of the gravitational field of the Earth. With the hypothesis that the distance between the centre of mass of the satellite and its elementary unit of mass is negligible with respect to the distance between the Earth and the satellite, it was possible to model the gravity gradient using equation (7).

$$\underline{M}_{G.G.} = 3n^2[\underline{c} \times I\underline{c}] \quad (7)$$

Where  $\underline{c}$  represents the direction cosines of the radial direction in the principal inertia axis. And  $n = \frac{Gm_{\oplus}}{r^3}$  is the mean angular velocity of the orbit.

### 5.2. Solar Radiation Pressure

The solar radiation which illuminates the faces and panels of the spacecraft generates a pressure that is not aligned with the centre of mass of the satellite, hence generating a disturbing torque. By taking into consideration only the effects of the specular reflection, diffuse reflection, and absorption whilst substituting their relationship, equation (8) was obtained.

$$\underline{F}_i = -PA_i(\widehat{S}_B \cdot \widehat{N}_{Bi})[(1 - \rho_s)\widehat{S}_B + (2\rho_s(\widehat{S}_B \cdot \widehat{N}_{Bi}) + \frac{2}{3}\rho_d)\widehat{N}_{Bi}] \quad (8)$$

Which was evaluated only when the solar radiation direction was directed towards the positive normal to the surface.

$$\underline{M}_{SRP} = \begin{cases} \sum_{i=1}^{N_{faces}} \underline{r}_i \times \underline{F}_i & \text{if } \widehat{S}_B \cdot \widehat{N}_{Bi} > 0 \\ 0 & \text{if } \widehat{S}_B \cdot \widehat{N}_{Bi} \leq 0 \end{cases}$$

### 5.3. Magnetic Field

This disturbing torque is caused by the interaction of the residual dipole moment, due to the parasitic currents of the satellite and the external magnetic field of the Earth. Equation (9) was used to model its effect on the spacecraft.

$$\underline{M}_B = \underline{j}_b \times \underline{B} \quad (9)$$

The value of  $\underline{j}_b$  is assumed to be  $\underline{j}_b = [0.1 \ 0.1 \ 0.1]^T \text{ A m}^2$ , which in the literature is identified as the worst-case scenario.

The model to compute the magnetic field of the Earth was based on the evaluation of its potential function which was defined as a series expansion of spherical harmonics; however, for the computation of the intensity magnetic torque, the potential was expanded up to the index  $n = 1$  like shown in equation (10)

$$\underline{B}_N = \frac{R^3 \oplus H_0}{r^3} [3(\hat{r} \cdot \hat{m})\hat{r} - \hat{m}] \quad (10)$$

Where:

- $\underline{B}_N$  will be appropriately rotated in the body frame of the spacecraft for the correct calculation of the torque.
- $\underline{r}$  is the vector that represents the radial position of the spacecraft in orbit.
- $\underline{m}$  is the dipole vector of the approximated magnetic field.
- $H_0$  was obtained using equation (11); truncating and approximating the harmonic summation.

$$H_0 = \sqrt{(g_1^0)^2 + (g_1^1)^2 + (h_1^1)^2} \quad (11)$$

The coefficient values shown in Table 7 were taken from the International Geomagnetic Reference Field [6].

**Table 7: Coefficient values**

		DGRF 2020	
n	m	g	h
1	0	-29404.8	-
1	1	-1450.9	4652.5
2	0	-2499.6	-
2	1	2892.0	-2991.6
2	2	1677.0	-734.6
3	0	1363.2	-
3	1	-2381.2	-82.1
3	2	1236.2	241.9
3	3	525.7	-543.4

Even though the mission takes place in LEO, the simplified model is enough to compute the intensity of the magnetic field.

#### 5.4. Air Drag

The interaction between the residual air particles from atmosphere and the satellite causes aerodynamic forces, consequently a disturbing torque is generated. The effect of the lift is neglected, while the main source is the effect due to the drag. The approximated model shown in equation (12) follows the general behaviour of an aerodynamic force.

$$\underline{F} = \frac{1}{2} C_D \rho v_{rel}^2 (\widehat{v_{rel}} \cdot \hat{N}_{Bi}) \frac{v_{rel}}{v_{rel}} A_i \quad (12)$$

Where:

- $C_D$  is the drag coefficient which from the literature it is assumed to be  $C_D \cong 2.2$
- $\rho(h, t)$  is the value of the density of the atmosphere as a function of altitude and time. For its estimation the Exponential Atmospheric Model was implemented where the medium altitude of the orbit is:  $Altitude = r_p - R_{\oplus} = 880.7 \text{ km}$ . [7]



- By substituting the atmospheric model:  $\rho = 1.163 \cdot 10^{-14} \left[ \frac{kg}{m^3} \right]$
- $\underline{v}_{rel}$  is the relative velocity between the spacecraft and the Earth's atmosphere assumed to be rigidly rotating with the Earth.

### 5.5. Disturbances' Behaviour

The general behaviour of the disturbances in absence of control during one orbit period can be observed in Figures 4.

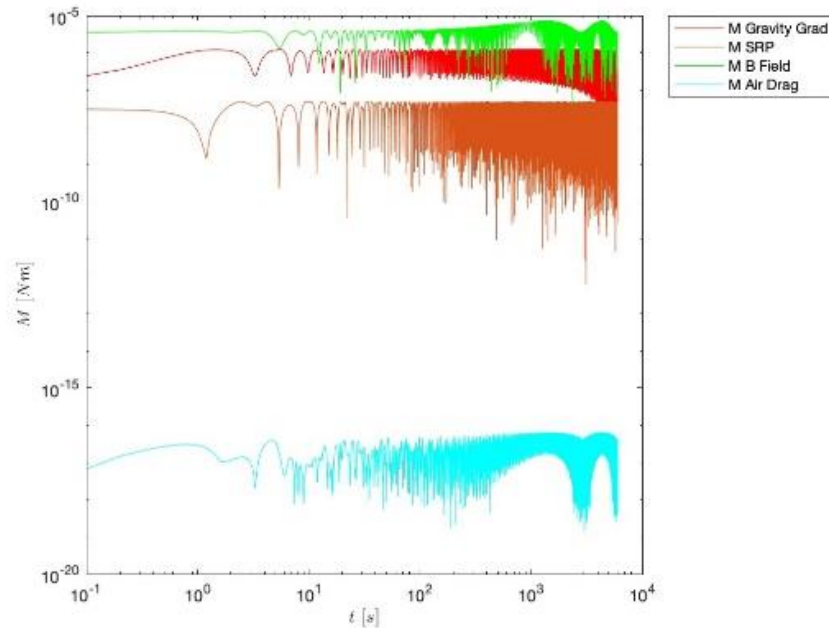


**Figure 4: All disturbing Torques.**

Figure 4 shows that the two most relevant sources for the mission are the gravity gradient and the magnetic field. The two sources shown in Figure 5 are indeed the ones considered in the final model for the simulation.

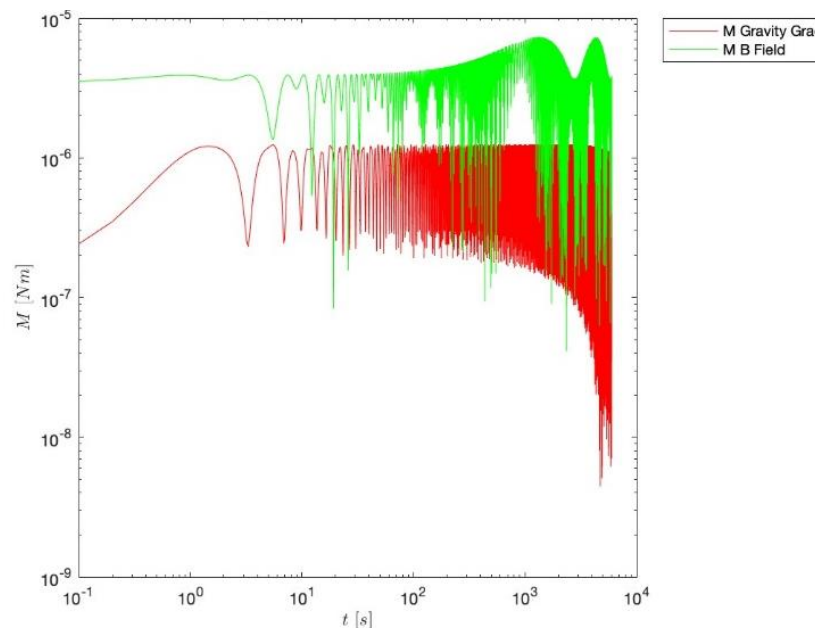


**Figure 5: Principal Disturbing Torques**

## 6. Attitude Sensing

The spacecraft can access the data in environment using sensors. This allowed for the determination of the attitude of the satellite itself by the on-board computer. To solve for the attitude matrix at least two vector measurements are needed, because of this, sun sensors and horizon sensors were added to the spacecraft. The sensors which have been included and their quantity can be seen in Table 8.[8]

**Table 8: Selected Sensors**

Sensor Type	Quantity	Mounting Direction
Gyroscope	3	+ X-axis
		+ Y-axis
		+ Z-axis
Horizon Sensor	1	- X-axis
Sun Sensor	6	+ X-axis
		- X-axis
		+ Y-axis
		- Y-axis
		+ Z-axis
		- Z-axis

### 6.1. Gyroscopic Sensors

The gyroscopes have been mounted in the principal axes directions to capture all three components of the angular velocity.

The model included a mounting error which has been assumed to be a rotation matrix obtained from small misalignment angles.

The gain was assumed to be unitary but subjected to random noise with zero mean value. Moreover, the noises have been modelled as white gaussian noises with the values given by the manufacturer catalogue [9]. The data for the selected gyroscope is shown in Table 9.

**Table 9: Gyroscope data**

Model	ARW (deg/√h)	RRW (deg/h <sup>3/2</sup> )	Dimension (mm)	Mass (g)	Resolution (deg/s)	Bandwith (Hz)
NSGY-001 Stellar Gyro	0.003	0.0015	37x35.5x49	55	1/60	20

Due to the high noise in the measurement, gyroscopes are not included the Attitude determination algorithm.

### 6.2. Horizon Sensors

Even though the orbit has a low eccentricity, a scanning horizon sensor was selected to compute the position of the centre of the planet with respect to the satellite with spherical coordinates.

For this reason, the white noise was added directly in the measurement of the spherical angles. The mean value was computed from the accuracy of the sensor as stated by the manual [10]. The data for the selected horizon sensor is shown in Table 10.

**Table 10:Horizon sensor data**

Model	Accuracy (deg)	Resolution (deg)	Dimension (mm)	Mass (g)	Bandwith (Hz)
GEN1-CubeSense	1/80	0.15	41.7x17.7x22.9	30	1

### 6.3. Sun Sensors:

Six sun sensors were added to compute the direction of the Sun from the spacecraft point of view. Like previously mentioned in the orbit characteristics, the selected orbit avoids any eclipse phase in which the spacecraft wouldn't be able to see the sun.

The same reasoning that allowed the modelling of the Horizon Sensor and its noise was implemented for these, where the ladder was also computed from the accuracy [11]. The data for the modelled sun sensors is shown in Table 11.

**Table 11:Sun sensor data**

Model	Accuracy (deg)	Resolution (deg)	Dimension (mm)	Mass (g)	Bandwith (Hz)
CSS-10	1/80	0.06	20x10x5.7	0.5	1

## 7. Attitude Determination

The measured unit vectors were processed to retrieve information on the orientation of the satellite during the whole mission.

Starting from the two unit-vectors measured from the horizon sensor and the sun sensor, the Algebraic algorithm was implemented to calculate an additional orthogonal direction and compute the orientation matrix between the body frame and the inertial reference frame.

To validate the model, an error matrix was defined by comparing the measured orientation matrix with the DCM from the kinematics.

From the error matrix, the non-diagonal terms and the diagonal ones were extracted, and the statistical analysis shown in Table 12 and 12 was conducted.

**Table 12:Gaussian Analysis for extra-diagonal components of error matrix**

	A_err_23	A_err_13	A_err_12	A_err_32	A_err_31	A_err_21
mean	2.03E-06	-8.62E-07	-6.98E-06	-2.02E-06	8.64E-07	6.99E-06
CL (68.3%)	4.79E-07	5.82E-07	5.54E-07	4.79E-07	5.82E-07	5.54E-07

**Table 13: Gaussian Analysis for diagonal components of error matrix**

	A_err_11	A_err_22	A_err_33
mean	1.00	1.00	1.00
CL (68.3%)	3.15E-10	2.70E-10	2.86E-10

The results in the Table 12 and Table 13 show that the error matrix could be treated as a rotation matrix composed of small angles with a confidence interval of 68.3% over a sample size of  $n = 1001$  values.

Such dimensions of the sample size allowed for a gaussian approximation of the behaviour.

## 8. Actuator Modelling

Actuators are required to provide a torque to the spacecraft to correct or change its orientation in space. This project makes use of momentum exchange techniques by means of control moment gyroscopes: spinning rotors with a constant angular velocity ( $h_r$ ) and gimbals that can be tilted by an angle ( $\delta$ ) and commanded to regulate the angular momentum of the platform.

The addition of actuators adds terms to the equation for the dynamics of the system. The change in orientation of the spin axis ( $\dot{A}$ ) and the assumption that the inertia properties of the system are not changing ( $\dot{I}\omega = 0$ ), lead to the formulation of equation (13).

$$I\dot{\omega} + \omega \times I\omega + \dot{A}h_r + \omega \times Ah_r = T \quad (13)$$

The CMG have been modelled following a pyramid configuration, in which the four gimbal axes are tilted equally of an angle ( $\beta = 0.9553 \text{ rad}$ ) with respect to the base plane. With this configuration,  $\dot{\delta}$  is calculated with equation (14).

$$\dot{\delta} = -B^* [M_c + \omega \times A \square_r] \quad (14)$$

$$\text{Where } Ah_r = \begin{bmatrix} -\cos(\beta) \sin(\delta_1) & -\cos(\delta_2) & \cos(\beta) \sin(\delta_3) & \cos(\delta_4) \\ \cos(\delta_1) & -\cos(\beta) \sin(\delta_2) & -\cos(\delta_3) & \cos(\beta) \sin(\delta_4) \\ \sin(\beta) \sin(\delta_1) & \sin(\beta) \sin(\delta_2) & \sin(\beta) \sin(\delta_3) & \sin(\beta) \sin(\delta_4) \end{bmatrix}$$

$$\text{and } B = h_r \begin{bmatrix} -\cos(\beta) \sin(\delta_1) & \sin(\delta_2) & \cos(\beta) \cos(\delta_3) & -\sin(\delta_4) \\ -\sin(\delta_1) & -\cos(\beta) \sin(\delta_2) & \sin(\delta_3) & \cos(\beta) \cos(\delta_4) \\ \sin(\beta) \cos(\delta_1) & \sin(\beta) \sin(\delta_2) & \sin(\beta) \cos(\delta_3) & \sin(\beta) \sin(\delta_4) \end{bmatrix}$$

To avoid losing the control capacity when B is approaching the singularity, a null command  $k\dot{\delta}_n$  was set to the actuators, where  $B\dot{\delta}_n = 0$  and  $k$  was given a value of  $-1$ . This causes a realignment of the actuators in such a way that they can be effective.

The VEOWARE microCMG shown in Figure 6 was used as reference for the actuators specifications shown in Table 14 [12].

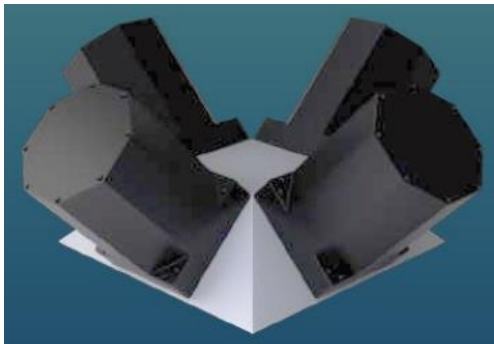


Figure 6: VEOWARE microCMG

Momentum (Nms)	0.7
Momentum 4 CMG (Nms)	2.3
Torque (Nm)	1.1
Torque 4 CMG (Nm)	3.5
Volume (mm <sup>3</sup> )	97x97x189
Mass (kg)	2.4

Table 14:CMG data

## 9. Attitude Control

From the point of view of the control, the mission was divided into three parts:

- De-tumbling
- Slew Manoeuvre
- Earth Pointing

Each of those phases was subjected to a different control logic which depended on the conditions of the phase itself.

The various states were derived from the measured quantities of the sensors. Specifically, the angular velocities were obtained from the gyroscopes and the attitude from the before mentioned algorithm in paragraph 7.

### 9.1. De-tumbling

For the first phase after the release from the launcher, the satellite must decrease its angular velocity from the initial conditions until the angular velocities are cancelled.

The initial conditions in terms of orientation were assumed to be large 312 Euler Angles with respect to the desired attitude, as the initial orientation was unknown.

The control logic shown in equation (15) has been implemented with a proportional control on the state which was only defined by the error in terms of the angular velocity with respect to the desired one. The ladder was imposed to be a null vector.

$$\underline{u}_{De-tumbling} = k_d (\underline{w}_m - \underline{w}_d) \quad (15)$$

Where:

- $\underline{u}$  : the control torque which was given as input to the actuators to effectively drive the spacecraft to the desired values.
- $\underline{w}_m$  was measured from the gyroscopic sensors.
- $\underline{w}_d$  was the desired angular velocity:  $\underline{w}_d = [0; 0; 0]$ .

The time given for the first phase was:  $t_{De-tumbling} = 50 \text{ s}$ , as it needed to decrease its velocity in the minimum possible time window so it could deploy the solar panels and recharge its batteries [13].

Both the sun sensors and the horizon sensor were switched off during this phase and immediately switched on after the batteries were recharged.

The actuators did not reach the saturation point, which allowed for the desaturation modelling to be omitted.

### 9.2. Slew-Manoeuvre

Once the De-tumbling phase was completed, the satellite needed to re-orient itself to start the actual scientific mission, coinciding with the last phase.

In order to accomplish the task, a Slew-Manoeuvre was performed to align the body frame with the LHLV reference frame, as the former had a random orientation due to the operation performed in phase one of the mission.

Furthermore, the time it took for the batteries to be recharged was neglected during the simulation and from this phase onwards, since the panels were deployed, the inertia of the panels was added to the one of the satellite.

To guarantee the continuity between the De-tumbling and the Slew-Manoeuvre models, the latter initial conditions were defined from the terminating values of the former.

The implemented control logic is shown in equation (16): a proportional control where the state was composed of the attitude error and the error in terms of angular velocity.

$$\underline{u}_{Slew-Manoeuvre} = k_p (A_e^T - A_e)^V + k_d (\underline{w}_m - \underline{w}_d) \quad (16)$$

Where:

- $A_e$  was the attitude error matrix, obtained from:  $A_e = A_m A_t^T$  as  $A_m$  was computed from the attitude determination while  $A_t$  was the target matrix coincident to the orientation of the LHLV frame with respect to the inertial frame.
- $\underline{w}_m$  was the angular velocity of the LHLV frame:  $\underline{w}_d = [0; 0; \dot{\theta}]$ , as  $\dot{\theta}$  was obtained from the model of the derivation of the true anomaly.

The time of simulation was set to:  $t_{Slew-Manoeuvre} = 500$  s as the Slew-Manoeuvre required more time to be completed.

### 9.3. Earth Pointing

Once the Slew-Manoeuvre is completed, the satellite is oriented towards the desired orientation. With this last phase, the control logic was designed to guarantee a stable precise pointing for the rest of the scientific mission.

The control logic was derived from the Lyapunov function which took into consideration, as shown in equation (17), both the attitude error and the angular velocity error.

$$V = \frac{1}{2} \underline{w}_e^T I_{tot} \underline{w}_e + 2k_p \text{tr}(I - A_e) \quad (17)$$

Where  $\underline{w}_e = \underline{w}_m - \underline{w}_d$ , and  $\underline{w}_d = [0; 0; \dot{\theta}]$  as the satellite must track the LHLV frame.

From such equation, the asymptotically stable control law of equation (18) was derived:

$$\underline{u}_{Earth-Pointing} = k_d \underline{w}_e + k_p (A_e^T - A_e)^V + \underline{w}_m \times I_{tot} \underline{w}_m + I_{tot} (A_e \dot{\underline{w}}_d - [\underline{w}_e^\wedge] A_e \underline{w}_d) \quad (18)$$

However, it was assumed that due to the low value in the eccentricity of the orbit the variation of the  $\underline{w}_d$  was negligible. So, equation (18) was simplified to the control law which was implemented (equation (19)) as a combination of both linear and non-linear control.

$$\underline{u}_{Earth-Pointing} = k_d \underline{w}_e + k_p (A_e^T - A_e)^V + \underline{w}_m \times I_{tot} \underline{w}_m - I_{tot} [\underline{w}_e^\wedge] A_e \underline{w}_d \quad (19)$$

The simulation time was coincident to one full orbital period:  $t_{Earth-Pointing} = T$

## 10. Block Diagram

The structure for the model described in the previous diagrams can be expressed as the block diagram shown in Figure 7.

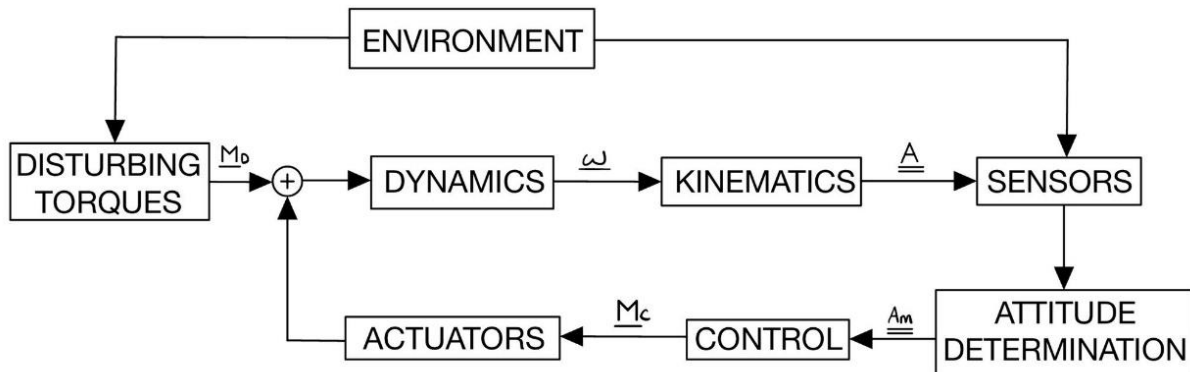


Figure 7: Block Model

## 11. Simulation Results

### 11.1. Pointing error, absolute pointing error and relative pointing error

The pointing error was defined with respect to the mission requirement which was Nadir Pointing. The analysis of the error was carried out only during the Earth Pointing phase as during the first two phases of the mission there is no target attitude to aim for.

A pointing error was also defined for the Slew-Manoeuvre; however, it was not included in the analysis. The results for the pointing error are presented in Table 15 and Figure 8.

Table 15: Pointing Error gaussian analysis.

	Mean [deg]	Variance [deg <sup>2</sup> ]	Std. Dev. [deg]	CL(68.3%) [deg]
Pointing Error	0.207	0.0186	0.136	0.000119

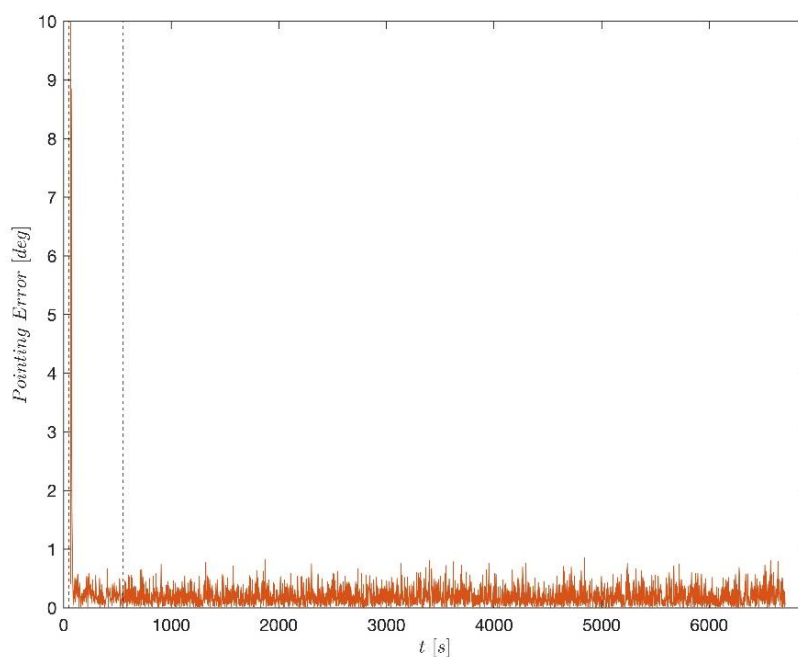


Figure 8: Pointing Error

The dashed lines in Figure 8, and in all the following ones, indicated the passage from one phase of the mission to the other, which implies a change in the control logic.

From the pointing error it was possible to evaluate the Absolute Pointing Error (APE) as the difference between the pointing error and the lower bound of the pointing requirement, which was the most stringent one and equal to  $0.1 \text{ deg}$ .

Furthermore, the Relative Pointing Error (RPE) was computed as the difference between the APE and the Mean Pointing Error (MPE) which was extracted from the ladder [14].

Both the APE and the RPE were subjected to a statistical analysis shown in Table 16, which was approximated to a gaussian behaviour.

**Table 16: Statistical analysis of APE and RPE**

	Mean [deg]	Variance [deg <sup>2</sup> ]	Std. Dev. [deg]	CL (68.3%) [deg]
<b>APE</b>	0.124	0.0145	0.121	0.000105
<b>PRE</b>	0.0940	0.0057	0.0755	0.0000658

Following this analysis, it was possible to state with a confidence level of 99.7% that both APE and RPE were confined in the intervals:

$$APE = 0.124 \pm 0.000153 \text{ deg} \text{ (Cl = 99.7\%)} \quad RPE = 0.0938 \pm 0.0000960 \text{ deg} \text{ (Cl = 99.7\%)}$$

Moreover, the same reasoning was applied to the pointing error which was:

$$Err_{Pointing} = 0.206 \pm 0.000173 \text{ deg} \text{ (Cl = 99.7\%)}$$

From such analysis it was possible to confirm that the pointing requirement was satisfied.

## 11.2. General results:

- I. De-Tumbling: Figure 9 shows how the angular velocity was decreased from the starting value given by the launcher mechanism.

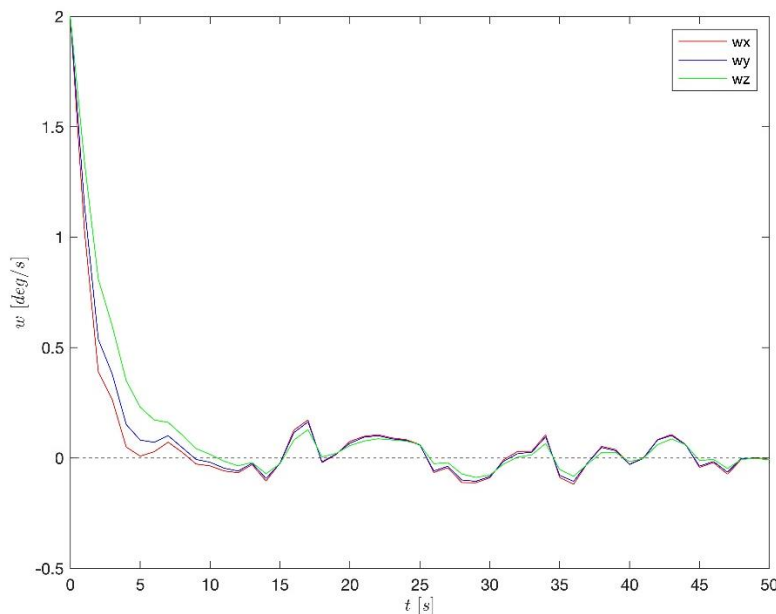


**Figure 9: Satellite angular velocity's components during De-tumbling**



- II. Slew-Manoeuvre: the attitude was brought from the general orientation at the end of the De-Tumbling to the desired one.

The behaviour of both the diagonal and the extra diagonal terms of the error matrix was determined to fully analyse the attitude of the Microsat. The terms were computed only in the second and last phase of the mission. These evolutions are shown in Figure 10 and Figure 11 respectively.

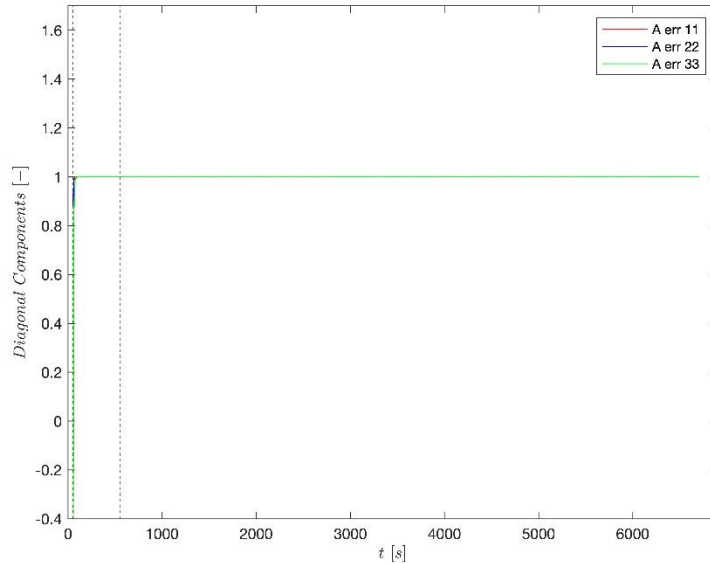


**Figure 10: Diagonal components of error matrix**

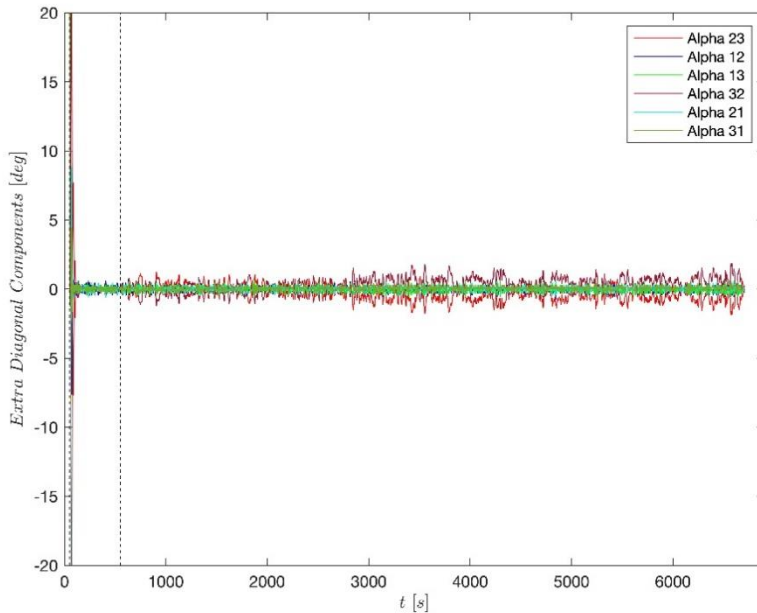


**Figure 11: Extra diagonal components of error matrix**

Both figures demonstrate how the error matrix between the LHLV frame, and the body frame converged to a rotation matrix composed of small Euler angles.

As a result, also the angular velocity of the satellite followed the one of the LHLV frame, which was  $\underline{w}_{HLV} = [0; 0; \dot{\theta}]$ ; this can be observed in Figure 12.

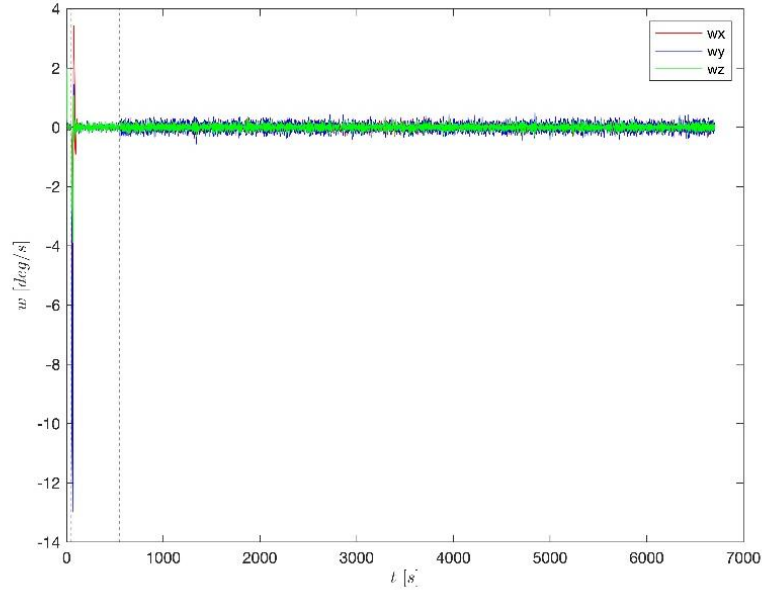


**Figure 12: Angular velocity**

In conclusion, the value of the torque provided by the actuators was computed. As Figure 13 shows, the saturation state is never reached during all the three phases. This means that the actuators are physically able to apply the torque set by the control action.

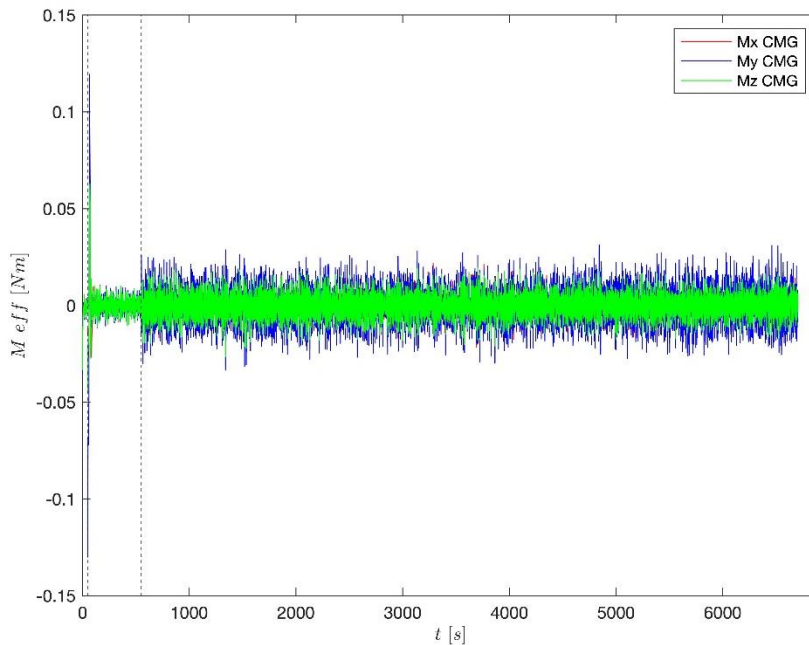


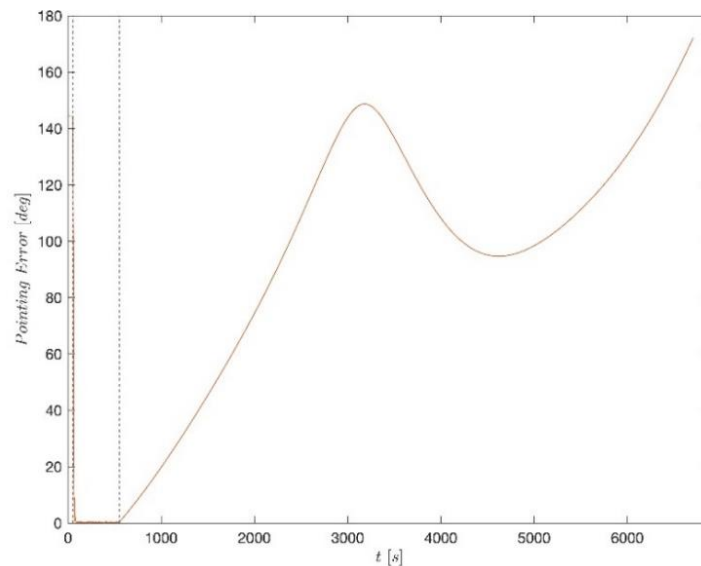
**Figure 13: Torque provided by the CMG.**

### 11.3. Uncontrolled simulation:

The last analysis was carried out for the Earth-pointing phase in the case of absence of the control logic and, consequently, of the actuator's action. The comparison between the controlled and uncontrolled cases was performed using initial conditions that coincide with the terminating ones of the Slew-Manoeuvre; results are shown in Table 17 and Figure 14.

**Table 17: Pointing error of uncontrolled pointing.**

	Mean [deg]	Variance [deg <sup>2</sup> ]	Std. Dev. [deg]	CL(68.3%) [deg]
<b>Pointing Error</b>	98.9	1751	41.8	0.0364

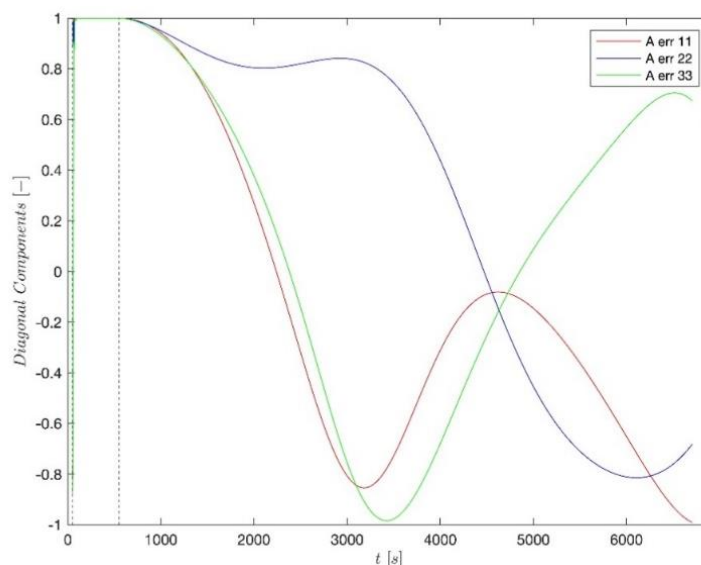
**Figure 14: Pointing error of uncontrolled pointing.**

The APE and RPE shown in Table 18 are once again computed with respect to the lower bound of the pointing requirement.

**Table 18: APE and RPE for uncontrolled pointing.**

	Mean [deg]	Variance [deg <sup>2</sup> ]	Std. Dev. [deg]	CL (68.3%) [deg]
<b>APE</b>	98.8	1750	41.8	0.0364
<b>PRE</b>	32.4	698	26.4	0.0230

The results show that in the absence of the control the pointing error would be unfit: with a confidence level of 99.7% the interval still does not match the required pointing conditions. The same reasoning was applied for the extra-diagonal components and the diagonal ones of the attitude error matrix. These components are shown in Figures 15 and 16.

**Figure 15: Diagonal components of uncontrolled error matrix**

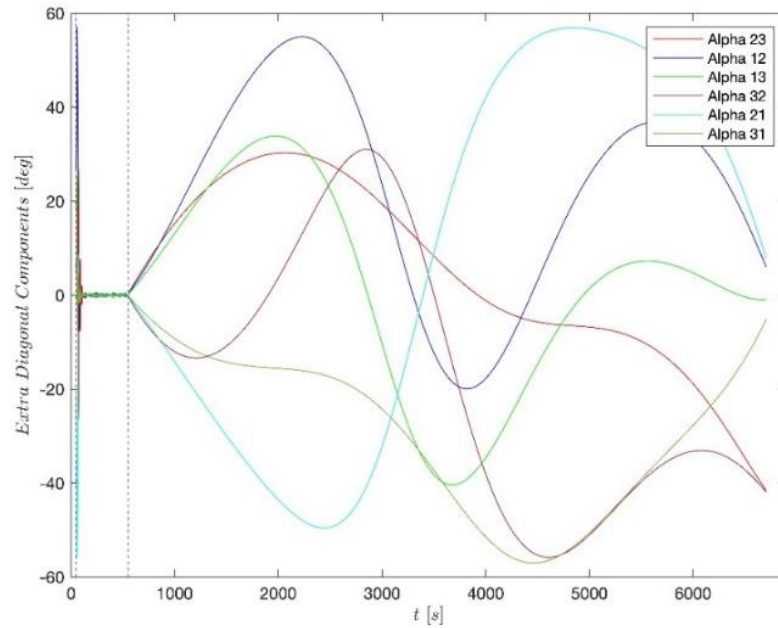


**Figure 16: Extra diagonal components of uncontrolled error matrix**

From Figures 15 and 16 it can be deduced that the approximation to a small Euler angle matrix for this condition is not valid, as there is no anti-symmetry behaviour between the extra-diagonal components and the diagonal ones diverged from the unitary value.

This uncontrolled behaviour was reflected on the angular velocity whose components did not follow the desired ones. The evolution of the angular velocities in this condition is shown in Figure 17.

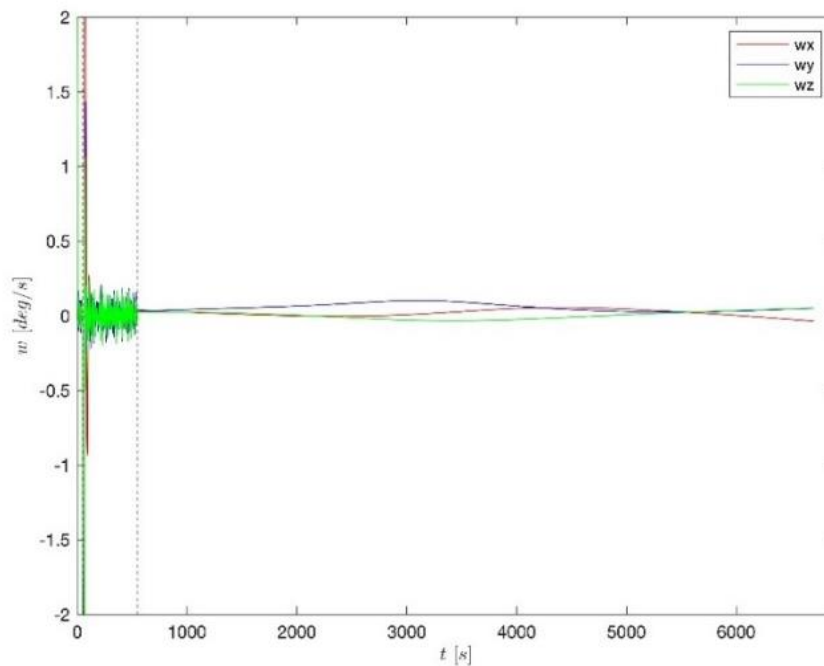


**Figure 17: Uncontrolled angular velocity components**

## 12. Conclusion

In conclusion, the undertaken project focuses on simulating the behaviours and designing a control loop for a Microsatellite for Earth observation. To achieve this, gyroscopes, sun sensors and horizon sensors were modelled, and control moment gyroscopes were used as actuators. The spacecraft kinematics were computed with the use of Euler angles, and the two sources of disturbing torques taken into consideration have been the gravity gradient and the magnetic field of the Earth.

The mission was composed by three phases:

- I. De-Tumbling: the satellite is released on its orbit with the angular velocity given by the launcher mechanism, and it must be slowed down to almost null angular velocity.
- II. Slew-Manoeuvre: the satellite had to move from its generic pointing at the end of the phase one, to the nominal pointing required for the last phase of the mission.
- III. Earth-Pointing: the satellite was controlled to satisfy the pointing requirement for the rest of the mission.

For those tasks to be accomplished, the model of the satellite was tested with three different control logic depending on the condition of the mission at hand:

- I. Proportional control directly on the state composed of the error in the angular velocity of the body:

$$\underline{u}_{De-tumbling} = k_d (\underline{w}_m - \underline{w}_d)$$

- II. Proportional control on the state composed of both the angular velocity error and the attitude error, as the Slew-Manoeuvre can be treated as rest-to-rest motions:

$$\underline{u}_{Slew-Manoeuvre} = k_p (A_e^T - A_e)^V + k_d (\underline{w}_m - \underline{w}_d)$$

- III. Combination of both linear and non-linear control to track the LHLV moving reference frame:

$$\underline{u}_{Earth-Pointing} = k_d \underline{w}_e + k_p (A_e^T - A_e)^V + \underline{w}_m \times I_{tot} \underline{w}_m - I_{tot} [\underline{w}_e^\wedge] A_e \underline{w}_d$$

The results of the simulation showed that the pointing requirement was satisfied in terms of both APE and RPE in the controlled case throughout the mission, as they never exceeded the boundaries of the requirement with a confidence level of 99.7%.

Furthermore, the error matrix between the LHLV frame and body frame demonstrated that the Microsat's attitude converged to the desired one. Also, this result was reflected on the behaviour of the angular velocity of the Microsat.

While in case of an uncontrolled simulation which was performed only during the pointing phase, the results showed that the pointing requirement was not respected as both the APE and RPE intervals were always over the required band with a confidence level of 99.7%. These results implied the necessity of the control during the mission.

### 13. References:

- [1] F. Landis Markley, John L. Crassidis, "Fundamentals of Spacecraft Attitude Determination and Control".
- [2] Arianespace. Vega User's Manual. Issue 04, April 2014. [Online]. Available: [https://www.arianespace.com/wp-content/uploads/2018/05/Vega-Users-Manual\\_Issue-04\\_April-2014.pdf](https://www.arianespace.com/wp-content/uploads/2018/05/Vega-Users-Manual_Issue-04_April-2014.pdf)
- [3] eoPortal. LAPAN-A2. [Online]. Available: <https://www.eoportal.org/satellite-missions/lapan-a2#performance-specifications>
- [4] Sparkwing. Satellite Solar Panels. [Online]. Available: <https://sparkwing.space/satellite-solar-panels/>
- [5] <http://www.ece.northwestern.edu/local-apps/matlabhelp/toolbox/simulink/slref/integrator.html>
- [6] NASA CCMC. Efieldtool. Version 1.1. [Online]. Available: <https://ccmc.gsfc.nasa.gov/models/efieldtool~1.1>
- [7] AIAA. " Design and Evaluation of a Semi-Empirical Piece-wise Exponential Atmospheric Density Model for CubeSat Applications," in Proceedings of the AIAA Conference, 2015. [Online]. Available: <https://arc.aiaa.org/doi/pdf/10.2514/6.2015-1589>
- [8] V. Pesce, A. Colagrossi, S. Silvestrini, "Modern Spacecraft Guidance, Navigation and Control", pp.253-336,2022.
- [9] NewSpace Systems. NSGY-001 Stellar Gyro. [Online]. Available: <https://satsearch.co/products/newspace-systems-nsgy-001-stellar-gyro>
- [10] CubeSpace. CubeSense N. [Online]. Available: <https://satsearch.co/products/cubespace-gen1-cubesense-n>
- [11] TensorTech. CSS-10 Coarse Sun Sensor. [Online]. Available: <https://satsearch.co/products/tensortech-css-10-coarse-sun-sensor>
- [12] Veoware Space. Micro CMG. [Online]. Available: <https://satsearch.co/products/veoware-space-micro-cmg>
- [13] F. Aghili, "Time-Optimal Detumbling Control of Spacecraft", Journal of Guidance, Control, and Dynamics, Vol.32, No.5, September-October 2009 [Online]. Available: [https://www.researchgate.net/publication/245433723\\_Time-Optimal\\_Detumbling\\_Control\\_of\\_Spacecraft](https://www.researchgate.net/publication/245433723_Time-Optimal_Detumbling_Control_of_Spacecraft)
- [14] M. Casasco et al., "Pointing Error Engineering Framework for High Pointing Accuracy Missions" in Proceedings of the ISSFD Conference, Year, [Online]. Available: [http://peet.estec.esa.int/files/ISSFD24\\_Paper\\_S15-2\\_Salehi.pdf](http://peet.estec.esa.int/files/ISSFD24_Paper_S15-2_Salehi.pdf)